Synergic effect of metal and fluorine doping on the structural and electrical properties of $La_{5.4}MoO_{11.1}$-based materials

Adrián López-Vergara[1], Marta Bergillos-Ruiz[1], Javier Zamudio-García[1], José M. Porras-Vázquez[1,], Jesús Canales-Vazquez[2], David Marrero-López[3], Enrique R. Losilla[1]*

1 Universidad de Málaga, Dpto. de Química Inorgánica, Cristalografía y Mineralogía 29071-Málaga, Spain

2 Renewable Energy Research Institute, University of Castilla-La Mancha, 02071-Albacete, Spain

3 Universidad de Málaga, Dpto. de Física Aplicada I, 29071-Málaga, Spain

KEYWORDS: hydrogen separation membrane, lanthanum molybdate, fluorination, polymorphism

ABSTRACT: Cationic and anionic frameworks of $La_{5.4}MoO_{11.1}$ proton conductors have been modified by means of metal (Ti^{4+}, Zr^{4+} and Nb^{5+}) and fluorine (F^-) doping. This synergic effect leads to the stabilization of high symmetry and single phase polymorphs. The materials have been fully characterized by structural techniques, such as X-ray and neutron powder diffraction and transmission electron microscopy. Fluorine content was determined by ion chromatography.

Impedance spectroscopy analysis under different atmospheres (dry and wet N_2, O_2 and wet 5% H_2-Ar) showed an improvement of the electronic conductivity under reducing conditions, making these materials potential candidates for hydrogen separation membranes.

1. Introduction

Nowadays, lanthanide molybdates ($Ln_{6-x}MoO_{12-\delta}$, Ln = La-Lu) are attracting attention as potential candidates for hydrogen separation membranes due to their mixed ionic-electronic conductivity[1-8]. Among the advantages of these materials are their stability towards CO_2 environments, unlike the traditional proton conductors based on $BaCeO_{3-\delta}$, unstable in CO_2 atmospheres and high water partial pressures, a key aspect to consider when the hydrogen is obtained through the reforming of hydrocarbons or water splitting, repectively[9-11].

Regarding the phase structure, it has been reported that for large rare-earth cations, such as La^{3+}, these compounds adopt a rhombohedral symmetry (s.g. $R\bar{3}$); for intermediate sizes, such as Sm^{3+}, Gd^{3+}, and Dy^{3+}, a cubic fluorite-type structure (s.g. $Fm\bar{3}m$); and for the smaller ones, such as Ho^{3+}, Er^{3+}, Tm^{3+}, Yb^{3+} and Lu^{3+}, a cubic bixbyite-type structure (s.g. $Ia\bar{3}$)[7]. In terms of synthesis-sintering conditions, recently our research group has carried out a comprehensive study of the $La_{6-x}MoO_{12-\delta}$ ($0 \leq x \leq 0.8$) series, and the influence of the synthesis temperature and cooling rate on the crystal structure of the samples[12]. Materials quenched from 1500 ºC crystallize in a simple cubic fluorite-type structure, whereas those cooled at slower rates, such as 50 and 0.5 ºC min^{-1}, are rhombohedral polymorphs with two different superstructures relative to a basic unit cell, denoted as R1 (7×7×1) and R2 (5×5×1), respectively. These results are in agreement with those published by Savvin *et al.*[8] where *in situ* neutron diffraction studies for $La_{5.5}MoO_{11.25}$ between 800

and 1400 ºC showed a reversible phase transition from a rhombohedral symmetry to a cubic fluorite at ~1270 ºC.

Cation doping is the most commonly used strategy to modulate the structure and improve the properties of advanced materials, e.g. the ionic conductivity. Modification of the cationic framework of $La_{6-x}MoO_{12-\delta}$ through metal-doping on the molybdenum ($La_{5.4}Mo_{0.9}A_{0.1}O_{12-\delta}$, A = Ti, Zr and Nb) and lanthanum sites ($La_{5.3}B_{0.1}MoO_{11.05}$, B = Ca, Sr, and Ba) were recently carried out[13]. The best results were obtained for Nb-doping, which leads to the stabilization of the R1 polymorph, regardless of the preparation conditions, in addition to an improvement of the densification and electrical properties. All the remaining samples present secondary phases and/or mixture of R1 and R2 polymorphs.

A novel approach to optimise the structural/electrical properties is the modification of the anionic framework by substituting O^{2-} by other anions such as F^-. This strategy has rendered excellent results for: i) cuprates, such as Ca_2CuO_3 or Sr_2CuO_3, leading to structural changes and an improvement of the superconducting properties[14-16]; ii) perovskite-type materials such as $SrFeO_{3-\delta}$, $La_{1-x}Sr_xFeO_{3-\delta}$, $SrCo_{0.9}Fe_{0.1}O_{3-\delta}$ and $BaFeO_{3-\delta}$, modifying the structure, magnetic properties and an enhancement of the oxygen transport[17-21]; iii) brownmillerite-type materials such as $Ba_2In_2O_5$[22-23], improving the ionic conductivity; iv) lanthanum molybdenum-doped tungstates, such as $La_{5.5}W_{0.6}Mo_{0.4}O_{11.25-\delta}$, resulting in improved chemical stability and hydrogen permeability[24].

In this context, the aim of this work is to study the combined effect of the modification of the cationic (Ti^{4+}, Zr^{4+} and Nb^{5+} doping) and anionic (F^- doping) frameworks on the structural and electrical properties of $La_{5.4}MoO_{11.1}$-based materials. The structural and microstructural

characteristics of these materials was studied by X-ray powder diffraction (XRPD), neutron powder diffraction (NPD), and transmission and scanning electron microscopy (TEM and SEM). The electrical characterization was carried out by impedance spectroscopy under different atmospheres.

2. Experimental

2.1. Synthesis

Materials with composition $La_{5.4}Mo_{1-x}A_xO_{12-\delta}$ (x = 0 and 0.1; A = Ti^{4+}, Zr^{4+} and Nb^{5+}) were prepared by the freeze-drying precursor method, following the synthetic procedure detailed in a previous work for similar materials[25]. The starting reagents were: La_2O_3 (99.99%, Aldrich), MoO_3 (99.5%, Aldrich), $Ti[OCH(CH_3)_2]_4$ (99%, Aldrich), $ZrO(NO_3)_2 \cdot 6H_2O$ (99%, Aldrich), and $Nb(HC_2O_4)_5 \cdot H_2C_2O_4$ (97%, ABCR). The precursor solutions were prepared by dissolving separately La_2O_3 in diluted nitric acid, MoO_3 in diluted ammonia, $Ti[OCH(CH_3)_2]_4$ in absolute ethanol, and $ZrO(NO_3)_2 \cdot 6H_2O$ and $Nb(HC_2O_4)_5 \cdot H_2C_2O_4$ in distilled water. An ethylenediaminetetraacetic acid solution (EDTA, 99.99%, Aldrich) was added as a complexing agent in a molar ratio 1:1 with respect to the total metal content. The different cation solutions were mixed in stoichiometric amounts under stirring, obtaining transparent solutions with a concentration of approximately 0.1 mol L^{-1} and pH=7. The solutions were frozen into liquid nitrogen and then dehydrated in a Scanvac-Coolsafe freeze-dryer for 2 days. The dried precursor powders were firstly calcined at 300 ºC for pre-combustion of the organic material and then at 800 ºC for 1 h to remove the remaining carbonaceous species and achieve crystallization.

In order to prepare the fluorinated materials, $La_{5.4}Mo_{1-x}A_xO_{12-y/2-\delta}F_y$, precursors powders previously calcined at 800 ºC were mixed with an stoichiometric amount of PVDF ($-CH_2-CF_2-$,

Aldrich), optimized by studying three different molybdate/PVDF molar ratios, $La_{5.4}MoO_{11.1-y/2}F_y$ (y = 1, 3 and 6). This fluorinating agent is preferred over a flow of F_2 gas, permitting the substitution of oxygen by fluorine at lower temperatures without the strong oxidising effect of F_2 gas and its concomitant hazards[26].

The corresponding mass of PVDF and lanthanum molybdate powders were ground for 15 min in an agate mortar and then calcined in air at 360 ºC for 12 h with heating and cooling rates of 1 and 5 ºC min^{-1}, respectively. Finally, all powders were compacted into pellets with 10 and 1 mm of diameter and thickness, respectively; and sintered between 1200 and 1500 ºC for 1 h with a heating rate of 10 ºC min^{-1} and different cooling rates. The obtained pellets were finely ground into powder for structural characterisation. Hereafter, all samples are labelled as A_x-T-F_y, where A and x are the dopant and cation content, respectively, T is the sintering temperature and y is the fluorine content. Samples without metal doping will be labelled as Mo-T-F_y.

2.2. Structural characterisation

All samples were analysed by laboratory X-ray powder diffraction (XRPD) by using a PANalytical Empyrean diffractometer with CuK$\alpha_{1,2}$ radiation. The acquisition time was approximately of 4 h over the 2θ angular range of 10-120º. The phase identification and structural analysis were performed using the X'Pert HighScore Plus and GSAS software[27,28].

Room temperature neutron diffraction (NPD) patterns were collected on the HRPT diffractometer using the SINQ neutron source at the Paul Scherrer Institut, (Villigen, Switzerland). The neutron wavelength, ~1.15 Å, was selected by the 511 reflection of the vertically focusing Ge monochromator and the samples were loaded in a vanadium can. The overall measurement time

was 6 h per pattern in order to obtain good statistics over the 2θ range of 13–150° (5–0.6 Å) with a step size of 0.05°.

The crystal structure was further investigated by selected area electron diffraction (SAED) and high-resolution transmission electron microscopy (HRTEM). The measurements were performed on a Jeol JEM 2100 electron microscope operating at 200 kV. TEM images were analysed using the Digital Micrograph™ software from Gatan[29].

Raman spectroscopy was performance with a JASCO NRS-5100 spectrometer by using an excitation line of 532 nm (Nd:YVO_4 laser), a power of 4.6 mW, and an acquisition time of 60 min.

The morphology and composition of the ceramic pellets were investigated by field emission scanning electron microscopy (FEI-SEM, Helios Nanolab 650), combined with energy dispersive spectroscopy (EDS, Oxford Instruments). The average grain size was estimated from the linear intercept method with the Estereologia software[30].

The fluorine content was determined by ion chromatography with a Metrosep column and the MagIC software. ~0.05 g of fluorinated sample was digested with 1 ml of HNO_3 and 3 ml of HCl in a Ultrawave digester (Milestone). A calibration curve was made with a certificated reference standard (E3A7.K1.W.L1, supplied by CPA Chem) for anions (F^-, Cl^-, Br^-, NO_3^-, PO_4^{3-} and SO_4^{2-}). Detection and quantification limits were of 11 and 37 ppb, respectively, well below the measured fluorine contents for the samples, in the order of the ppm.

2.3. Electrical characterisation

Impedance spectra were acquired using a frequency response analyser (Solartron 1260 FRA) in dry and wet (2 vol.% H_2O) N_2 and O_2 and wet 5% H_2-Ar. The data were collected in the

0.01 Hz to 1 MHz frequency range with an ac perturbation of 100 mV on cooling from 800 to 200 °C and a dwell time of 30 min at each measurement temperature. Pt current collectors were formed by coating the pellet surfaces with Pt-ink (METALOR® 6082) and then fired at 800 ºC for 1 h in air. The data were simulated by equivalent circuit models using the ZView program[31].

3. Results and discussion

3.1. Optimisation of fluorine content, sintering temperature and cooling rate of $La_{5.4}MoO_{11.1-\delta}$

In order to analyse the influence of the sintering temperature, $La_{5.4}MoO_{11.1-y/2}F_y$ with y = 3 was calcined between 800 and 1500 ºC for 1 h with a cooling rate of 5 ºC min^{-1} (Figure 1). The XRPD pattern of the precursor fluorinated at 360 ºC is also shown. A dramatic change can be observed respect to the unfluorinated materials [Figure 1 in reference 12]. At temperatures lower than 1100 ºC, broad diffraction peaks are observed due to the nanocrystalline nature of the powders. In addition, La_2MoO_6 is detected as secondary phase in the temperature range 800-1100 ºC, decreasing as the sintering temperature increases. At 1200 ºC the sample present a pseudo-cubic symmetry without the evidence of minor secondary phases, i.e. La_2O_3, R1 or R2. A deep inspection of the XRPD pattern reveals a splitting of the diffraction peaks (inset Figure 1), indicating that is not fully cubic. At sintering temperatures between 1300 and 1400 ºC, the samples are a mixture of rhombohedral polymorphs, and the R1 phase is only stabilized at 1500 ºC (see next paragraph). These results indicate that fluorination, and the concomitant modification of the anionic framework, has a significant effect on the polymorphism of lanthanum molybdates. It has to be mentioned that no F-containing species are detected in the whole range of temperatures, likely due to the incorporation of fluorine to the different phases.

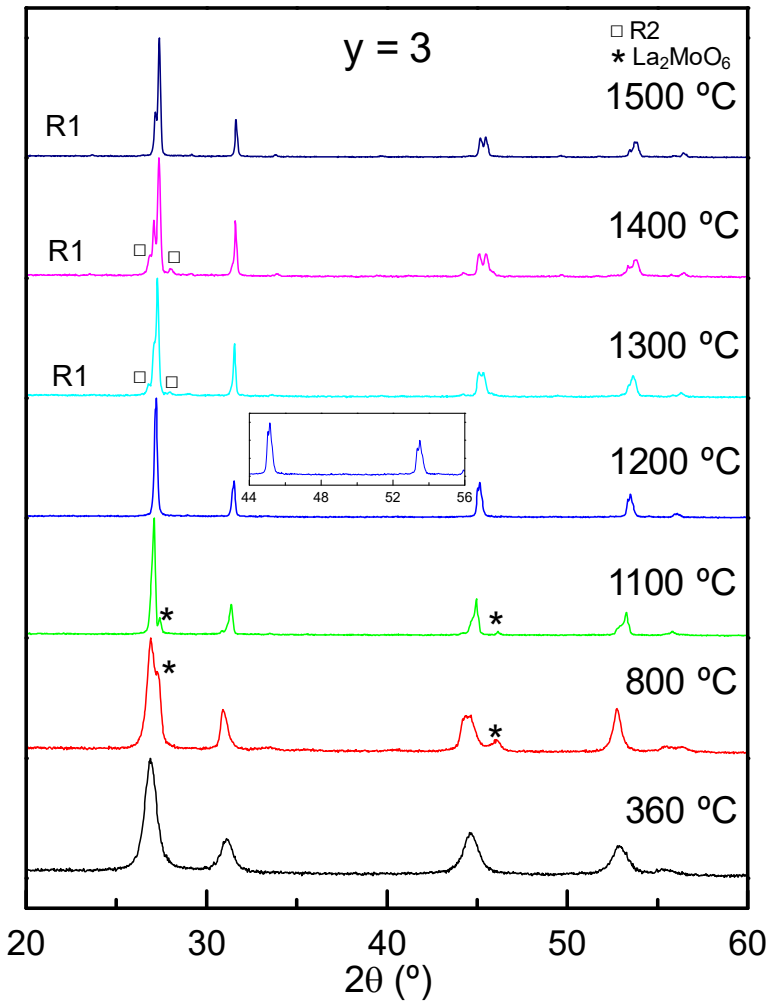

Figure 1. XRPD patterns of $La_{5.4}MoO_{11.1-y/2}F_y$ (y = 3) sintered between 360 and 1500 ºC for 1 h and cooled down at 5 ºC min^{-1}.

XRPD patterns of $La_{5.4}MoO_{11.1-y/2}F_y$ (y = 0, 1, 3 and 6) obtained at 1500 ºC for 1 h with a cooling rate of 5 ºC min^{-1} are shown in Figure S1a. As can be seen, the fluorinated sample with y = 3 crystallizes as a single phase with the R1 structure, unlike the undoped sample, where a small amount of the R2 polymorph is detected. Higher contents of fluorine (y = 6) lead to minor segregations of R2 and La_2O_3. In contrast, for the lowest amount of fluorine (y = 1), no changes are observed compared to the unfluorinated compound (y = 0).

Finally, the impact of the cooling rate (quenching, 50, 5 and 0.5 ºC min^{-1}) on the polymorphic stabilization is also investigated (Figure S1b). For the quenched sample, the cubic symmetry is obtained and for the remaining cooling rates the R1 polymorph is stabilized, whereas for non-fluorinated samples, at a cooling rates lower than 50 ºC min^{-1}, R1+R2 or R2 phases are obtained.[12] Bearing in mind these results, the amount of fluorine and cooling rate that will be used henceforth are y = 3 and 5 ºC min^{-1}, respectively, experimental conditions that are easily reproducible in any laboratory and lead to single phase compounds at 1200 and 1500 ºC.

3.2. Influence of fluorination on cation-doped $La_{5.4}Mo_{0.9}A_{0.1}O_{12-\delta}$ (A = Ti^{4+}, Zr^{4+} and Nb^{5+})

In order to examine the fluorine incorporation into cation-doped lanthanum molybdates[13], $La_{5.4}Mo_{0.9}A_{0.1}O_{12-y/2-\delta}F_y$ (A = Ti, Zr and Nb, y = 0 and 3), fluorinated precursors were heated between 1200 and 1500 ºC for 1 h and cooled down at 5 ºC min^{-1} (Figure 2 and S2).

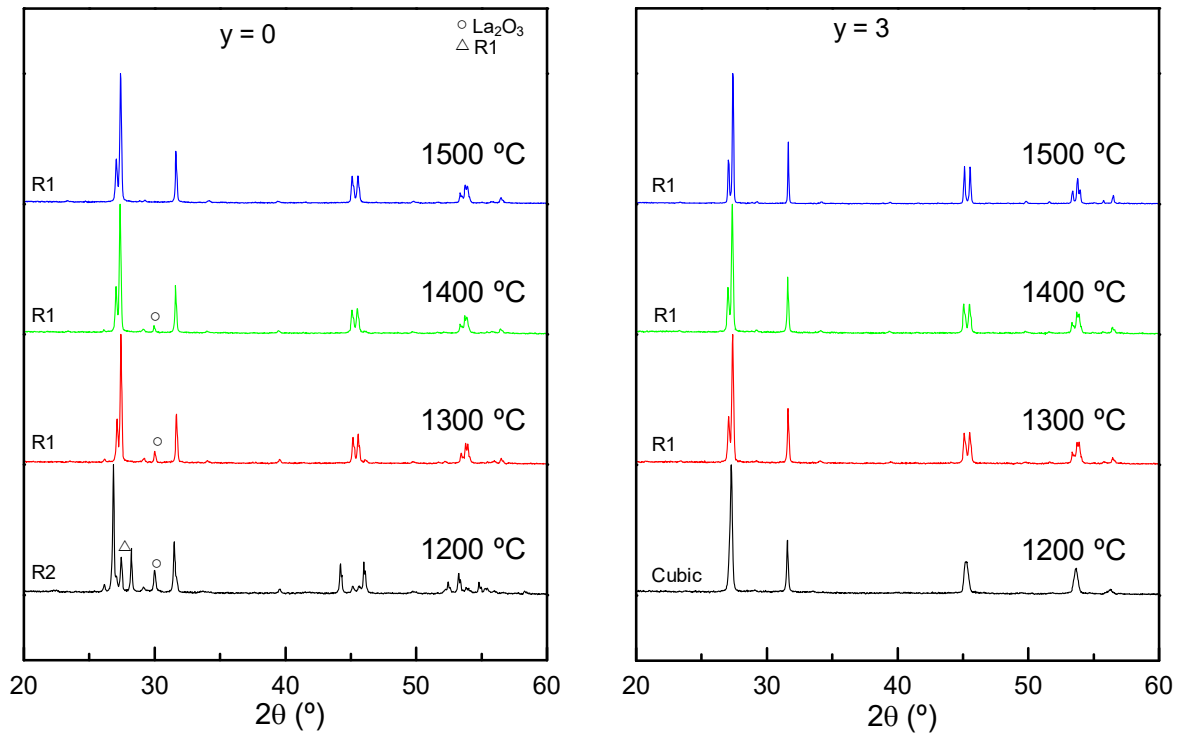

Figure 2. XRPD patterns of $La_{5.4}Mo_{0.9}Nb_{0.1}O_{11.05-y/2-\delta}F_y$ (y = 0 and 3) sintered between 1200 and 1500 ºC for 1h and cooled down at 5 ºC min^{-1}. The majority phase for each sample is denoted at the bottom left of the diffraction patterns and the minor secondary phases are labelled.

For all cation-doped compounds, a structural change is observed between the non-fluorinated samples, dominated by the presence of the R1 and R2 polymorphs and La_2O_3, and the fluorinated ones, where single phases are obtained at sintering temperatures lower than 1500 ºC. It is important to mention that for $Nb_{0.10}$-1200-F0, a mixture of R1, R2 and La_2O_3 is detected, not observed for $Ti_{0.10}$-1200-F0 and $Zr_{0.10}$-1200-F0, where only R2 and La_2O_3 are present, indicating that Nb-doping by itself already leads to the formation of the R1 polymorph. The most remarkable result was obtained for $Nb_{0.10}$-1200-F3, where a cubic fluorite-type structure is stabilized. Ti and Zr-doping, in the same sintering conditions, result in the formation of multiphasic samples (Figure S2). Moreover, it has to be mentioned that Mo-1200-F3 did not possess a fully cubic symmetry (Figure 1), making evident the synergic effect of the modification of both cationic and anionic sublattices on the crystal structure. Higher sintering temperatures, from 1300 to 1500 ºC, for cation-doped samples, lead to single phases with a R1 symmetry without evidence of La_2O_3, as it occurs for the non-fluorinated materials (Figure 2 and S2).

3.3. Structural analysis by X-ray and neutron powder diffraction and transmission electron microscopy

Rhombohedral samples obtained between 1300-1500 ºC, $La_{5.4}Mo_{1-x}A_xO_{12-y/2-\delta}F_y$ (x= 0, 0.1; A = Ti, Zr, Nb; y = 3) were analysed by the Le Bail method due to the lack of a structural model. Parameters such as unit cell, scale factor, background and peak shape coefficients were refined. An example of the fitting for Mo-1500-F3 is shown in Figure 3a and results of Le Bail refinement are given in Table 1. As can be observed, the most intense diffraction peaks, corresponding to the

basic unit cell, are adequately fitted; however, the smaller ones, attributed to the superstructure reflections are not adjusted. This will be further discussed in the TEM section.

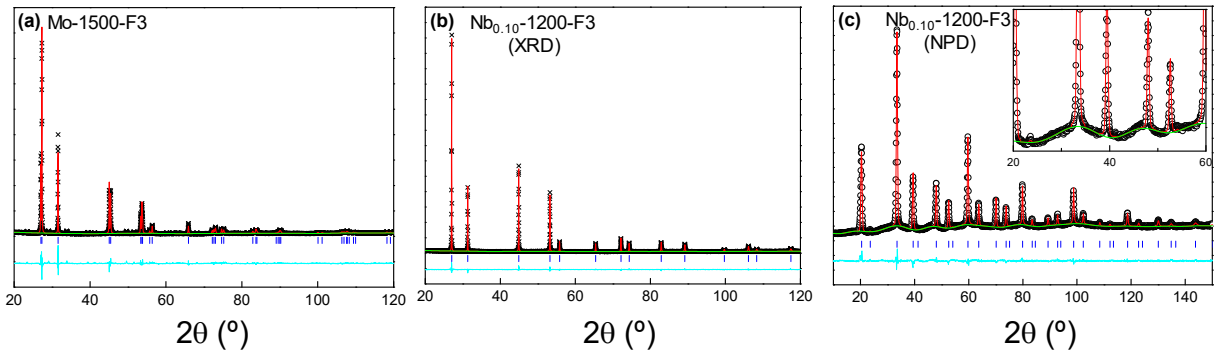

Figure 3. (a) XRPD pattern refined by the Le Bail method for $La_{5.4}MoO_{11.1-y/2}F_y$ (y = 3) sintered at 1500 ºC; (b) XRPD pattern refined by the Rietveld method for $La_{5.4}Mo_{0.9}Nb_{0.1}O_{11.05-y/2-\delta}F_y$ (y = 3) sintered at 1200 ºC; (c) neutron powder diffraction pattern refined by the Rietveld method for $La_{5.4}Mo_{0.9}Nb_{0.1}O_{11.05-y/2-\delta}F_y$ (y = 3) sintered at 1200 ºC. [Observed data (circles), calculated pattern (continuous line), and difference curve (bottom)].

Regarding the unit cell parameters, a decrease of the cell volumes is observed at 1500 ºC for the cation-doped samples compared to the undoped specimen (Mo-1500-F3). This is the expected behaviour, since the ionic radii of Mo^{6+} (with an ionic radius of 1.02 Å in an 8-fold coordination[13]) is substituted by other cations with smaller ionic radii, Ti^{4+} (0.74 Å), Zr^{4+} (0.84 Å) and Nb^{5+} (0.74 Å). It is important to mention that Ti and Nb-doped samples, despite their same ionic radii, have different cell volumes. This behaviour is likely due to fact that the aliovalent substitution of Mo^{6+} by Ti^{4+} leads to the formation of an oxide vacancy per mole of dopant. However, Nb^{5+} only generates half vacancy per mole, leading to a higher oxygen content and, hence, a larger cell volume.

Table 1. Unit cell parameters and agreement factors determined from XRPD by Le Bail method for $La_{5.4}Mo_{1-x}A_xO_{12-y/2-\delta}F_y$ (x= 0, 0.1; A = Ti, Zr, Nb; y = 3) heated at 1300-1500 ºC for 1 h and cooled down at 5 ºC·min^{-1}. Average grain sizes, D, determined from SEM images are also shown.

	a (Å)	c (Å)	V/Z(Å^3)	R_{wp} (%)	D (μm)
Mo-1500-F3	3.9938(2)	9.8693(5)	45.44(1)	9.62	30
$Ti_{0.10}$-1300-F3	3.9956(2)	9.9110(5)	45.68(1)	8.65	6.2
$Ti_{0.10}$-1400-F3	3.9901(1)	9.8937(4)	45.47(1)	9.12	12.1
$Ti_{0.10}$-1500-F3	3.9808(1)	9.8801(1)	45.20(1)	8.53	16
$Zr_{0.10}$-1300-F3	3.9949(1)	9.9077(5)	45.64(1)	9.31	4.9
$Zr_{0.10}$-1400-F3	3.9893(1)	9.8952(5)	45.46(1)	8.56	15.6
$Zr_{0.10}$-1500-F3	3.9845(1)	9.8834(1)	45.30(1)	7.32	18
$Nb_{0.10}$-1300-F3	3.9940(1)	9.8853(5)	45.52(1)	9.57	4.3
$Nb_{0.10}$-1400-F3	3.9919(1)	9.8835(5)	45.46(1)	9.93	13.4
$Nb_{0.10}$-1500-F3	3.9851(1)	9.8938(3)	45.36(1)	6.23	20.9

On the other hand, when samples are heated at lower final temperatures, 1400 and 1300 ºC, an increase in cell volumes is observed (Table 1) due to the higher incorporation of fluorine at low temperatures (see below). This increase can be explained taking into account that to preserve the lattice electroneutrality during the fluorination reaction, one oxygen has to be replaced by two fluorines, increasing the anion content. The extra fluorine anion is incorporated into an oxide vacancy position of the lattice, leading to an enlargement of the electrostatic repulsion in the anionic network.[32]

Fluorine content was quantified by ion chromatography (Table 2), detecting a low incorporation with respect to the theoretical value added (~ 16 at.% for y = 3), a fact that is accentuated when the sintering temperature increases due to F evaporation. For instance, $Nb_{0.10}$-1200-F3 and $Nb_{0.10}$-1300-F3 present a fluorine content of 0.26 and 0.034 wt. %, respectively. For higher sintering temperatures the fluorine content is below the detection limit of the technique. In addition, bearing in mind these results, the chemical formulas have been recalculated in order to

take into consideration the fluorine incorporation, resulting for Mo-1200-F3 and $Nb_{0.10}$-1200-F3 experimental formulas of $La_{5.4}MoO_{11.077}F_{0.045}$ and $La_{5.4}Mo_{0.9}Nb_{0.1}O_{10.98}F_{0.14}$, respectively (Table 2).

Table 2. Atomic and weight concentrations of fluorine and experimental formulas for $La_{5.4}Mo_{1-x}A_xO_{12-y/2-\delta}F_y$ (x= 0, 0.1; A = Ti, Zr, Nb; y = 3) heated at 1200-1400 ºC for 1 h and cooled down at 5 ºC·min^{-1}.

	[F] at %	[F] wt %	Experimental formula
Mo-1200-F3	0.26	0.085	$La_{5.4}MoO_{11.077}F_{0.045}$
$Ti_{0.10}$-1300-F3	0.08	0.026	$La_{5.4}Mo_{0.9}Ti_{0.1}O_{10.993}F_{0.014}$
$Ti_{0.10}$-1400-F3	0.01	0.004	$La_{5.4}Mo_{0.9}Ti_{0.1}O_{10.998}F_{0.002}$
$Zr_{0.10}$-1300-F3	0.09	0.03	$La_{5.4}Mo_{0.9}Zr_{0.1}O_{10.992}F_{0.016}$
$Zr_{0.10}$-1400-F3	0.02	0.006	$La_{5.4}Mo_{0.9}Zr_{0.1}O_{10.998}F_{0.003}$
$Nb_{0.10}$-1200-F3	0.80	0.26	$La_{5.4}Mo_{0.9}Nb_{0.1}O_{10.98}F_{0.14}$
$Nb_{0.10}$-1300-F3	0.10	0.034	$La_{5.4}Mo_{0.9}Nb_{0.1}O_{11.041}F_{0.018}$
$Nb_{0.10}$-1400-F3	0.02	0.006	$La_{5.4}Mo_{0.9}Nb_{0.1}O_{11.048}F_{0.003}$

The local structure was examined by selected area electron diffraction (SAED) to confirm the results obtained by XRPD. Mo-1500-F3 shows intense reflections, which are reminiscent of the fluorite type structure; however, additional reflections are observed along certain crystallographic axis, indicating the formation of a supercell. The SAEDs patterns of this specimen have been indexed considering the basic rhombohedral unit cell determined by XRPD data (s.g. $R\bar{3}$, a=3.98 and c=9.88 Å). In the [001] zone axis a 7×7 superstructure of the basic unit cell is observed (Figure 4a); however, these superstructure reflections are not observed along the (003) direction (Figure 4b), indicating that the real cell is 7a×7a×c superstructure relative to the basic unit cell determined by XRPD. The corresponding HRTEM image shows evidence of this periodicity, in good agreement with the proposed superstructure (Figure 4c). On the other hand, $Nb_{0.10}$-1200-F3 shows the characteristic reflections of a cubic fluorite structure (s.g. $Fm\bar{3}m$) with lattice cell parameter of a_F = 5.6 Å (Figure 4d and e). The HRTEM images further confirm that

this sample is a cubic fluorite without visible formation of superstructures, modulations or clusters of defects (Figure 4f).

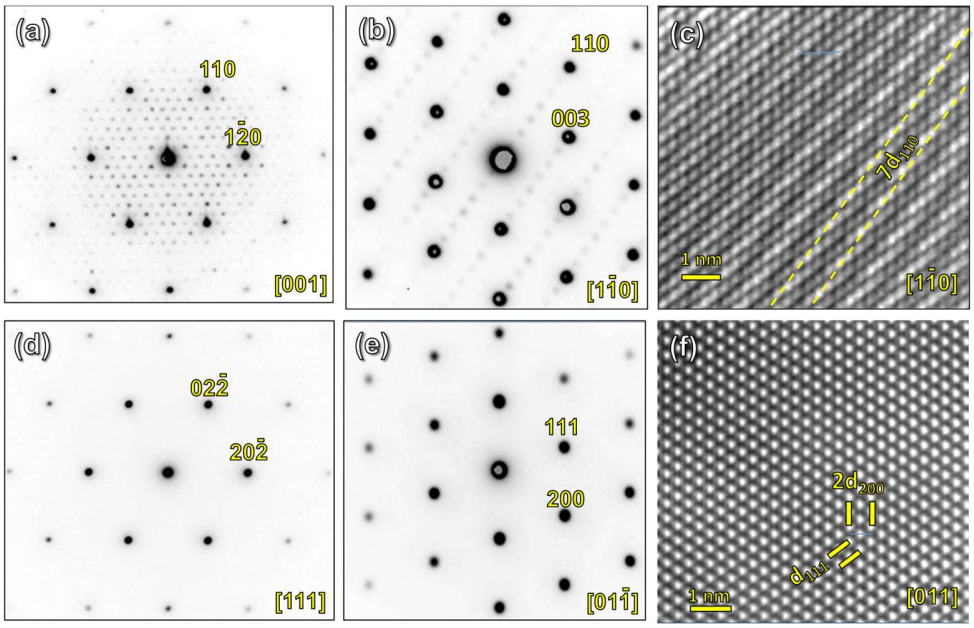

Figure 4. SAED patterns and HRTEM images of $La_{5.4}MoO_{11.1-y/2}F_y$ (y = 3) obtained at 1500 ºC (a, b, c) and $La_{5.4}Mo_{0.9}Nb_{0.1}O_{12-y/2-\delta}F_y$ (y = 3) sintered at 1200 ºC (d, e, f) in different zone axes.

The cubic sample obtained at 1200 ºC, $La_{5.4}Mo_{0.9}Nb_{0.1}O_{11.05-y/2-\delta}F_y$ (y = 3) was studied by a combined Rietveld refinement of XRPD and NPD data in order to confirm the symmetry after cation and anion doping. Data were also collected for the non-fluorinated analogue prepared at 1500 ºC and quenched from that temperature, named as $Nb_{0.10}$-1500-Q, for comparison. [13]

For all refinements, a single fluorite-type structure with a $Fm\bar{3}m$ space group was used as starting structural model. Occupancy factors were initially set to the nominal stoichiometry, where La, Mo and Nb were located in the same crystallographic positions and their isotropic displacement parameters constrained to be the same. Refinement of the occupancy factors led to values close to the theoretical ones, therefore, these were maintained. Fluorine was not included in the structural

model as oxygen and fluorine are not distinguishable by neutron powder diffraction. The same parameters mentioned above were refined, in addition to the isotropic displacement parameters. An example of the fitting for $Nb_{0.10}$-1200-F3 is shown in Figure 3b and 3c for XRPD and NPD data, respectively, and the parameters derived from these analyses are shown in Table 3.

Table 3. Unit cell parameters, agreement factors, atomic displacement, occupancy factors, O(F)-O(F) distances determined from combined XRPD-NPD Rietveld method for $La_{5.4}Mo_{0.9}Nb_{0.1}O_{11.05-y/2-\delta}F_y$ (y = 3) heated at 1200 ºC for 1h and cooled down at 5 ºC·min^{-1}. Average grain sizes, D, determined by SEM are also shown.

	$Nb_{0.10}$-1200-F3	**$Nb_{0.10}$-1500-Q**
a (Å)	5.6993(1)	5.6607(1)
V/Z(Å^3)	46.28(1)	45.35(1)
R_{wp}^{XRPD}/ R_{wp}^{NPD} (%)	4.00/3.96	4.99/3.89
R_F^{XRPD}/ R_F^{NPD} (%)	1.97/4.72	3.54/4.53
La/Mo/Nb, 4a, (0, 0, 0)		
Uiso × 100 (Å^2)	2.65(1)	2.58(1)
Occupancy factor La/Mo/Nb	0.7714(-)/ 0.1286(-)/0.0143(-)	0.7714(-)/ 0.1286(-)/0.0143(-)
O, 8c, (¼,¼,¼)		
Uiso × 100 (Å^2)	2.91(2)	4.84(5)
Occupancy factor	0.767(2)	0.732(3)
d O(F)-O(F) (Å)	2.85(1)	2.83(1)
D (μm)	1.2	33.5

The refinements are quite good with low disagreement factors. It is observed an expansion in the cell volume for the fluorinated sample in comparison with the non-fluorinated one, despite the size of F^- in a tetrahedral coordination, 1.31 Å, is lower than that of O^{2-} (1.38 Å) in the same environment. This is due to the replacement of 1 oxygen by 2 fluorine with the concomitant increase of the electrostatic repulsions in the anionic network, as discussed before for the rhombohedral samples heated at 1300-1500 ºC. The expansion of the unit cell due to electrostatic repulsions is further confirmed by analysing the O(F)-O(F) distances, which are larger in the anion

doped samples, Table 3. It has to be noted that the oxygen occupancy factors are lower than the theoretical ones, likely due to strong correlations with the atomic displacement parameters, whose high values reveal the local disorder of these materials in both cationic and anionic sublattices. This disorder is also displayed as an undulating background of the NPD pattern (inset of Figure 3c), as previously reported for related materials.[13] Regardless, it can be seen the tendency of an increase of the oxygen occupation factors of the fluorinated samples compared to the pristine ones, due to the filling of the oxygen vacancies of the structure by fluorine.

Raman spectroscopy has been carried out for $Nb_{0.10}$-1200-F3 in order to further prove that the phase obtained is a true fluorite, as it was previously stablished with XRPD, NPD and HR-TEM studies. Figure S3 shows a characteristic band centered at ~780 cm^{-1} assigned to the stretch vibration of the oxygen in a MoO_6 octahedron, similar to Sm_6MoO_{12}, also with a fluorite structure.[33] The bands centered at 330 and 410 cm^{-1} are related with the O-Mo-O bending motions.

3.4. Microstructural, phase stability under reducing conditions and electrical characterisation

The scanning electron microscopy images show that the pellets sintered at 1200 ºC (Figure S4) present some residual porosity with relative density about 90% as a consequence of the low sintering temperature used. The average grain size is 1.8 and 1.2 µm for Mo-1200-F3 and $Nb_{0.10}$-1200-F3, respectively (Table 1 and 3). For higher sintering temperatures, and the cation-doped samples, a clear increase of the average grain size is observed, where $Ti_{0.10}$-1500-F3, $Zr_{0.10}$-1500-F3 and $Nb_{0.10}$-1500-F3 present values of 16, 18 and 20.9 µm, respectively. EDS mapping reveals that the samples are chemically homogenous (Figure S5) without liquid phases or segregations.

In order to ensure the reliability of these materials under reducing conditions, and their application as hydrogen separation membranes, stability tests were only conducted for single phase compounds. The fluorinated samples were annealed at 800 ºC for 48 h under flowing 5% H_2-Ar and, afterwards, analysed by XRPD, Figure S6. The materials remain stable after the treatment in reducing conditions, maintaining a R1 or cubic symmetry. However, for Mo-1200-F3 and $Ti_{0.10}$-1500-F3, segregations of La_2MoO_6 and TiO_2 have been detected.

The conductivity of stable samples was studied under different atmospheres, dry/wet gases of N_2, O_2, and wet 5% H_2−Ar. Figure 5 shows representative impedance spectra for $Nb_{0.10}$-1500-F3 under the five flowing atmospheres. The spectra display only one contribution at high frequency, which is fitted by using the following equivalent circuit: (RQ), where R is a resistance in parallel with a constant phase element (Q). The real capacitance takes values of 5 pF cm^{-1}, which is clearly related to bulk conduction. Thus, no grain boundary contribution to the conductivity is detected for any sample or sintering temperature, likely due to the large grain size of the pellets as well as the absence of phase segregations at the grain boundary region.

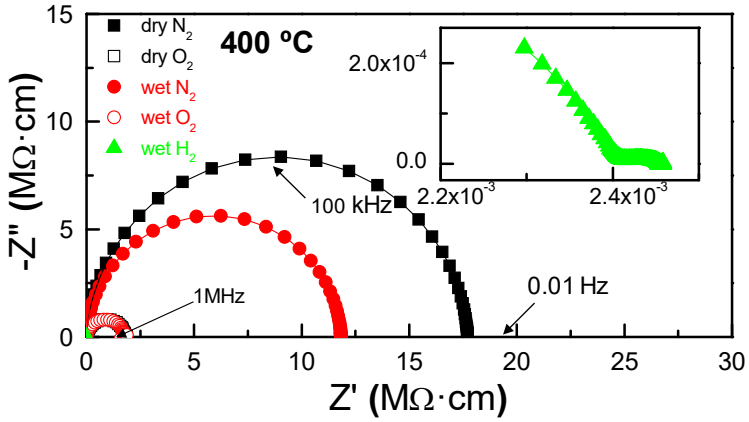

Figure 5. Representative impedance spectra of $La_{5.4}Mo_{0.9}Nb_{0.1}O_{12-y/2-\delta}F_y$ (y = 3) sintered at 1500 ºC under different flowing atmospheres at 400 °C.

The Arrhenius plots for $Nb_{0.10}$-1500-F3 show a very significant increase of the conductivity in wet N_2 and O_2 atmospheres compared to dry conditions, due to an important proton contribution to the overall conductivity at temperatures lower than 600 ºC (Figure 6). The increase of conductivity in O_2 compared to N_2 atmosphere is attributed to a small p-type electronic contribution to the overall conductivity. The same behaviour was already reported in previous works for non-fluorinated lanthanum molybdates[12,13].

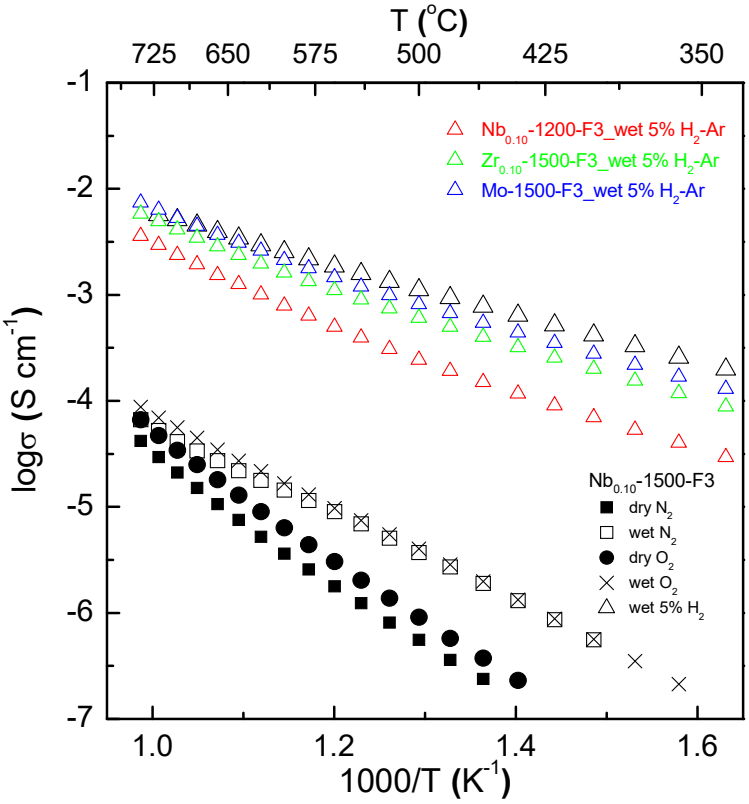

Figure 6. Arrhenius plots of the overall conductivity for $La_{5.4}Mo_{0.9}Nb_{0.1}O_{11.05-y/2-\delta}F_y$ (y = 3) sintered at 1500 ºC for 1 h and cooled down at 5 ºC min^{-1} under different flowing atmospheres. Other selected samples measured under wet 5% H_2−Ar are also shown.

Similar plots are observed for the remaining compositions. However, it has to be mentioned that a significant drop in conductivity is observed for $Nb_{0.10}$-1500-F3 with respect to the non-fluorinated Nb-doped sample [$Nb_{0.10}$_50 in reference 13] from 0.21 and 0.31 to 0.02 and 0.03 mS

cm^{-1} at 700 ºC, in dry N_2 and O_2, respectively. Moreover, for $Nb_{0.10}$_50, the activation energies in the low temperature range are 0.81 and 0.72 eV in dry and wet conditions, respectively, whereas for $Nb_{0.10}$-1500-F3 are 1.07 and 0.89 eV, respectively, in the same range. This drop in conductivity and activation energies increase might be due to the filling of the oxide vacancies by fluorine atoms, hindering the oxide ion conduction mechanism because of the loss of oxide vacancies as demonstrated by NPD studies. In reducing conditions, the conductivity increases due to a significant n-type contribution, caused by a minor reduction of Mo^{6+} to Mo^{5+}, reaching similar values to those reported for non-fluorinated samples in previous works[12,13], demonstrating that the small incorporation of fluorine into the anionic framework does not modify the molybdenum oxidation state.

Figure 6 also compares the Arrhenius plots for other cation-doped samples with rhombohedral symmetry and sintered at 1500 ºC. At temperatures lower than 600 ºC, $Nb_{0.10}$-1500-F3 exhibits slightly higher conductivity than Mo-1500-F3, with values of 1.1 and 0.81 mS cm^{-1}, respectively, at 500 ºC, due to a higher number of oxide vacancies. However, $Zr_{0.10}$-1500-F3 shows the lowest conductivity, 0.61 mS cm^{-1} at 500 ºC, likely due to a smaller average grain size (Table 1). Finally, $Nb_{0.10}$-1200-F3, despite its high symmetry, presents lower conductivity values that the other samples, 0.24 mS cm^{-1} at 500 ºC, likely due to its low sintering temperature and lower relative density, as mentioned in the microstructural section.

As further work, the preparation of the materials with high density and symmetry at low temperatures by means of the addition of sintering aids as CoO or ZnO will be considered. In addition, hydrogen permeability tests will be carried out in order to evaluate the suitability of these materials as hydrogen separation membranes.

CONCLUSIONS

Metal doped $La_{5.4}Mo_{1-x}A_xO_{12-y/2-\delta}F_y$ (x= 0, 0.1; A = Ti, Zr, Nb) were synthesized from freeze-dried precursors, where an optimised amount of fluorine (y = 3) was added, leading to the stabilization of high symmetry and single phase materials, not achieved for their non-fluorinated counterparts. Chemical analysis by ion chromatography demonstrated the successful incorporation of fluorine into the crystal structure The most remarkable result was obtained for $La_{5.4}Mo_{0.9}Nb_{0.1}O_{11.05-y/2-\delta}F_y$ (y = 3), which crystallizes with cubic symmetry, regardless the synthetic conditions used. The structural studies showed an increase of the cell volume for the fluorinated samples, caused by the replacement of 1 oxygen by 2 fluorine ions, augmenting the electrostatic repulsions in the anionic network and, hence, an expansion of the cell. These results were further confirmed by neutron diffraction studies, were oxygen/fluorine occupation factors were higher for the fluorinated samples in comparison to the non-fluorinated ones. TEM studies confirmed the changes in crystal symmetry. The stability tests showed that most of the fluorinated samples were stable under reducing conditions.

A marked decrease of the electrical properties is observed for the fluorinated samples in dry/wet N_2 and O_2 atmospheres, likely due to the filling of the oxide vacancies by fluorine, impeding the oxide conduction mechanism. However, a very significant increase of the conductivity is observed under reducing conditions due to a n-type electronic contribution as a consequence of the partial reduction of Mo^{6+} to Mo^{5+}.

ASSOCIATED CONTENT

Supporting Information: Additional experimental results, including SEM-EDS analysis of $La_{5.4}Mo_{0.9}Nb_{0.1}O_{12-y/2-\delta}F_y$ (y = 3) sintered at 1200 ºC; SEM micrographs for $La_{5.4}Mo_{1-x}Nb_xO_{12-y/2-}$

$_{\delta}F_y$ (x = 0, 0.1; y = 3) sintered at 1200 and 1500 ºC for 1 h; and XRPD patterns after experiments in reducing conditions at 800 ºC for $La_{5.4}Mo_{1-x}Nb_xO_{12-y/2-\delta}F_y$ (x= 0, 0.1; and y = 3)] and rhombohedral [$La_{5.4}Mo_{1-x}A_xO_{12-y/2-\delta}F_y$ (x= 0, 0.1; A = Ti, Zr, Nb; y = 3) samples, obtained at 1200 and 1500 ºC, respectively

AUTHOR INFORMATION

Corresponding Author

e-mail address: josema@uma.es (José Manuel Porras Vázquez)

Present address: Dpto. de Química Inorgánica, Cristalografía y Mineralogía, Facultad de Ciencias, Campus de Teatinos, Universidad de Málaga, 29071-Málaga, Spain.

Tel: +34 951953298

Author Contributions

The manuscript was written through contributions of all authors. All authors have given approval to the final version of the manuscript.

Funding Sources

This work was supported by Ministerio de Ciencia, Innovación e Universidades through the RTI2018-093735-B-I00 and MAT2016-77648-R and Junta de Andalucía through UMA18-FEDERJA-033 research grants (Spain). J.M.P.-V. thanks the University of Málaga for his funding. A. L.-V. thanks Junta de Andalucía and the European Social Fund for his Young Researcher Contract (UMAJI35).

ACKNOWLEDGMENT

We would like to thanks the SINQ facility (Paul Scherrer Institute) for the NPD time and Denis Sheptyakov for his help during the NPD experiments.

REFERENCES

(1) Chen, Y.; Liao, Q.; Li, Z.; Wang, H.; Wei, Y.; Feldhoff, A.; Caro, J. A CO_2-Stable Hollow-Fiber Membrane with High Hydrogen Permeation Flux. *AIChE*. **2015**, *61*, 1997–2007.

(2) Vøllestad, E.; Vigen, C. K.; Magrasó, A.; Haugsrud, R. Hydrogen permeation characteristics of $La_{27}Mo_{1.5}W_{3.5}O_{55.5}$. *J. Membrane Sci*. **2014**, *461*, 81–88.

(3) Escolástico, S.; Somacescu, S.; Serra, J. M. Tailoring mixed ionic–electronic conduction in H_2 permeable membranes based on the system $Nd_{5.5}W_{1-x}Mo_xO_{11.25-\delta}$. *J. Mat. Chem. A*. **2015**, *3*, 719–731.

(4) Amsif, M.; Magrasó, A.; Marrero-López, D.; Ruiz-Morales, J. C.; Canales-Vázquez, J.; Núñez, P. Mo-Substituted Lanthanum Tungstate $La_{28-y}W_{4+y}O_{54+\delta}$: A Competitive Mixed Electron−Proton Conductor for Gas Separation Membrane Applications. *Chem. Mater*. **2012**, *24*, 3868–3877.

(5) Savvin, S. N.; Shlyakhtina, A. V.; Borunova, A. B.; Shcherbakova, L. G.; Ruiz-Morales, J. C.; Núñez, P. Crystal structure and proton conductivity of some Zr-doped rare-earth molybdates. *Solid State Ion.* **2015**, *271*, 91−97.

(6) Shlyakhtina, A. V.; Savvin, S. N.; Knotko, A. V.; Shcherbakova, L. G.; Núñez, P. Electrical Conductivity of $Ln_{6-x}Zr_xMoO_{12+\delta}$ (Ln = La, Nd, Sm; x = 0.2, 0.6) Ceramics during Thermal Cycling. *Inorg. Mater*. **2016**, *52*, 1055−1062.

(7) Shlyakhtina, A. V.; Savvin, S. N.; Lyskov, N. V.; Kolbanev, I. V.; Karyagina, O. K.; Chernyak, S. A.; Shcherbakova, L. G.; Núñez, P. Polymorphism in the Family of $Ln_{6-x}MoO_{12-\delta}$ (Ln= La, Gd - Lu; x = 0, 0.5) Oxygen Ion- and Proton-Conducting Materials. *J. Mater.Chem. A* **2017**, *5*, 7618−7630.

(8) Savvin, S. N.; Avdeev, M.; Kolbanev, I. V.; Kharitonova, E. P.; Shcherbakova, L. G.; Shlyakhtina, A. V.; Nuñez, P. Stability against reduction of fluorite-like rhombohedral $La_{5.5}MoO_{11.25}$ and $Ho_{5.4}Zr_{0.6}MoO_{12.3}$ fluorite: Conductivity and neutron diffraction study. *Solid State Ion.* **2018**, *319*, 148−155.

(9) Medvedev, D.; Murashkina, A.; Pikalova, E.; Demin, A.; Podias, A.; Tsiakaras, P. $BaCeO_3$: Materials development, properties and application. *Prog. Mater. Sci*. **2014**, *60*, 72−129.

(10) Tao, Z. T.; Yan, L. T.; Qiao, J. L.; Wang, B. L.; Zhang, L.; Zhang, J. J. A review of advanced proton-conducting materials for hydrogen separation. *Prog. Mater. Sci*. **2015**, *74*, 1−50.

(11) Ruiz-Trejo, E.; Irvine, J. T. S. Ceramic proton conducting membranes for the electrochemical production of syngas. *Solid State Ion*. **2012**, *216*, 36−40.

(12) López-Vergara, A.; Porras-Vázquez, J. M.; Infantes-Molina, A.; Canales-Vázquez, J.; Cabeza, A.; Losilla, E. R.; Marrero-López, D. Effect of Preparation Conditions on the Polymorphism and Transport Properties of $La_{6-x}MoO_{12-\delta}$ ($0 \leq x \leq 0.8$). *Chem. Mater*. **2017**, *29*, 6966−6975.

(13) López-Vergara, A.; Porras-Vázquez, J. M.; Vøllestad, E.; Canales-Vázquez, J.; Losilla, E. R.; Marrero-López, D. Metal-Doping of $La_{5.4}MoO_{11.1}$ Proton Conductors: Impact on the Structure and Electrical Properties, *Inorg. Chem*. **2018**, *57*, 12811−12819.

(14) Al-Mamouri, M.; Edwards P. P.; Greaves, C.; Slaski, M. Synthesis and superconducting properties of the strontium copper oxy-fluoride $Sr_2CuOF_{2+\delta}$. *Nature* 1994, **369**, 382−384.

(15) Al-Mamouri, M.; Edwards P. P.; Greaves, C.; Slater, P. R.; Slaski, M. Synthesis and Structure of the Calcium Copper Oxyfluoride, $Ca_2CuO_2F_{2+\delta}$, *J. Mater. Chem*. **1995**, *5*, 913−916.

(16) Slater, P. R.; Hodges, J. P.; Francesconi, M. G.; Edwards, P. P.; Greaves, C.; Gameson, I.; Slaski, M. An improved route to the synthesis of superconducting copper oxyfluorides $Sr_{2-x}A_xCuO_2F_{2+\delta}$ (A = Ca, Ba) using transition metal difluorides as fluorinating reagents. *Physica C* **1995**, *253*, 16−22.

(17) Clemens, O.; Berry, F. J.; Wright, A. J.; Knight, K. S.; Perez-Mato, J. M.; Igartua, J. M.; Slater, P. R. A neutron diffraction study and mode analysis of compounds of the system $La_{1-x}Sr_xFeO_{3-x}F_x$ (x = 1, 0.8, 0.5, 0.2) and an investigation of their magnetic properties. *J. Solid State Chem.* **2013**, *206*, 158−169.

(18) Clemens, O.; Berry, F. J.; Bauer, J.; Wright, A. J.; Knight, K. S.; Slater, P. R. Synthesis, structural and magnetic characterisation of the fluorinated compound 15R-$BaFeO_2F$. *J. Solid State Chem.*, **2013**, *203*, 218−226.

(19) Zhang, Z.; Zhu, Y.; Zhong, Y.; Zhou, W.; Shao, Z. Anion Doping: A New Strategy for Developing High-Performance Perovskite-Type Cathode Materials of Solid Oxide Fuel Cells, *Adv. Energy Mater*. **2017**, *7*, 1700242.

(20) Dong, F.; Chen, Y.; Chen, D.; Shao, Z. Surprisingly High Activity for Oxygen Reduction Reaction of Selected Oxides Lacking Long Oxygen-Ion Diffusion Paths at Intermediate Temperatures: A Case Study of Cobalt-Free $BaFeO_{3-\delta}$. *ACS Appl. Mater. Interfaces* **2014**, *6*, 11180−11189.

(21) Zhu, J.; Liu, G.; Liu, Z.; Chu, Z.; Jin, W.; Xu, N. Unprecedented Perovskite Oxyfluoride Membranes with High-Efficiency Oxygen Ion Transport Paths for Low-Temperature Oxygen Permeation. *Adv. Mater*. **2016**, *28*, 3511−3515.

(22) Chen, L.; Zhuang, L.; Xue, J.; Wei, Y.; Wang, H. Tuning the separation performance of hydrogen permeable membranes using an anion doping strategy. *J. Mater. Chem. A* **2017**, *5*, 20482−20490.

(23) Animitsa, I.; Tarasova, N.; Filinkova, Ya. Electrical properties of the fluorine-doped $Ba_2In_2O_5$. *Solid State Ion.* **2012**, *207*, 29–37.

(24) Animitsa, I.; Tarasova, N. The influence of anionic heterovalent doping on transport properties and chemical stability of F-, Cl-doped brownmillerite $Ba_2In_2O_5$. J. Alloy. Compd. **2018**, *739*, 353–359.

(25) Porras-Vázquez, J. M.; dos Santos-Gómez, L.; Marrero-López, D.; Slater, P. R.; Masó, N.; Magrasó, A.; Losilla, E. R. Effect of tri- and tetravalent metal doping on the electrochemical properties of lanthanum tungstate proton conductors. *Dalton Trans*. **2016**, *45*, 3130−3138.

(26) Slater, P. R. Poly(vinylidene fluoride) as a reagent for the synthesis of K_2NiF_4-related inorganic oxide fluorides. *J. Fluorine Chem*. **2002**, *117*, 43−45.

(27) X'Pert HighScore Plus Program, Version 3.0e; PANalytical B.V.: Amelo, The Netherlands, 2012.

(28) Larson, A. C.; von Dreele, R. B. GSAS Program; Report LA-UR-86748; Los Alamos National Lab, 1994.

(29) Digital Micrograph, Version 3.22.1461.0; Gatan: Pleasanton, CA.

(30) Abrantes, J. C. C. Estereologiá, UIDM, ESTG; Polytechnic Institute of Viana do Castelo: Viana do Castelo, Portugal, 1998.

(31) Johnson, D. ZView: A Software Program for IES Analysis, Version 2.9c; Scribner Associates, Inc.: Southern Pines, NC, 2005.

(32) Slater, P. R.; Gover, R. K. B. Synthesis and structure of the new oxide fluoride $Ba_2ZrO_3F_2{\cdot}xH_2O$ (x~0.5) *J. Mater. Chem*. **2001**, *11*, 2035−2038.

(33) Shlyakhtina, A. V.; Savvin, S. N.; Lyskov, N. V.; Belov, D. A.; Shchegolikhin, A. N.; Kolbanev, I. V.; Karyagina, O. K.; Chernyak, S. A.; Shcherbakova, L.G.; Núñez, P. $Sm_{6-x}MoO_{12-\delta}$ (x = 0, 0.5) and Sm_6WO_{12} – Mixed electron-proton conducting materials *Solid State Ion*. **2017**, *302*, 143–151.

For Table of Contents Only

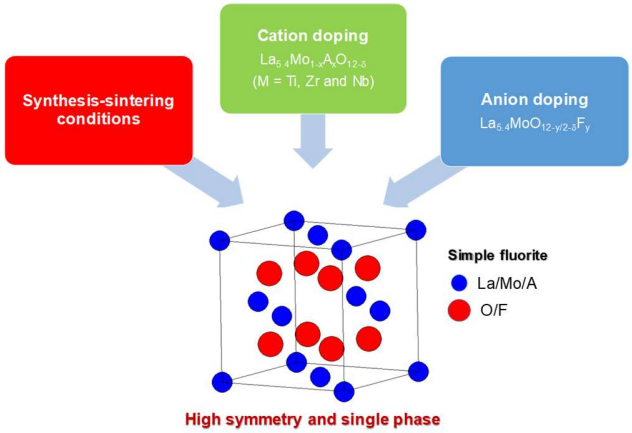

Table of Contents caption: The synergic modification of the cationic and anionic frameworks of $La_{6-x}MoO_{11.1}$-based materials leads to the stabilization of high symmetry and single phase samples.